Empirical formulation for debris flow impact and energy release

Di Perna, Angela; Cuomo, Sabatino; Martinelli, Mario

DOI
10.1186/s40677-022-00210-9

Publication date
2022

Document Version
Final published version

Published in
Geoenvironmental Disasters

Geoenvironmental Disasters

RESEARCH

Open Access

Empirical formulation for debris flow impact and energy release

Angela Di Perna[1], Sabatino Cuomo[1*] and Mario Martinelli[2,3]

Abstract

Full understanding the interaction mechanisms between flow-like landslides and the impacted protection structures is an open issue. While several approaches, from experimental to numerical, have been used so far, it is clear that the adequate assessment of the hydromechanical behaviour of the landslide body requires both a multiphase and large deformation approach. This paper refers to a specific type of protection structure, namely a rigid barrier, fixed to the base ground. Firstly, a framework for the Landslide-Structure-Interaction (LSI) is outlined with special reference to the potential barrier overtopping (nil, moderate, large) depending on the features of both the flow and the barrier. Then, a novel empirical method is casted to estimate the impact force on the barrier and the time evolution of the flow kinetic energy. The new method is calibrated by using an advanced hydro-mechanical numerical model based on the Material Point Method. The validation of the empirical formulation is pursued referring to a large dataset of field evidence for the peak impact pressure. Both numerical and empirical methods can appropriately simulate the physical phenomena. The performance of the newly proposed empirical method is compared to the literature methods and its advantages are outlined.

Keywords: Impact mechanisms, Mitigation, Structure, Material Point Method

Introduction

The interaction of flow-like landslides with rigid walls, obstacles, protection structures and, more recently, single building or cluster of buildings have been investigated by a variety of numerical tools. Either Discrete Element Method (DEM) (Teufelsbauer et al. 2011; Leonardi et al. 2016; Calvetti et al. 2017) or continuum mechanics has been adopted. For the latter, Eulerian methods were extensively applied (Moriguchi et al. 2009; Kattel et al. 2018), but Lagrangian methods such as Smoothed-Particle Hydrodynamics (SPH) (Pastor et al. 2009) and Material Point Method (MPM) (Bui and Fukagawa 2013; Cuomo et al. 2013; Ceccato et al., 2018) have a great potential. The massive use of numerical methods is related to the inner complexity of Landslide-Structure-Interaction (LSI) mechanisms, which are related to: (i) the hydro-mechanical features of the impacting flow, (ii) the geometry of the structure, and (iii) initial and boundary conditions for the specific LSI problem. Recently the solid–fluid hydro-mechanical coupling and the role of the interstitial fluid in the LSI mechanisms have been considered. For instance, the impact behaviour of saturated flows against rigid barriers (as observed in centrifuge tests) was satisfactorily simulated through MPM (Cuomo et al. 2021). Most of these approaches are very recent, and still need comprehensive validation combined with more efforts to reduce the computational cost, which is very high once realistic simulations are pursued.

A more traditional approach is based on (i) direct observation of the impact of flow-like landslides against barriers, and (ii) correlation of the achieved measurements. The measurements available in the literature have been mostly obtained in reduced-scale flume tests (Hübl et al. 2009; Armanini et al. 2011; Canelli et al. 2012; Ashwood and Hungr 2016; Vagnon and Segalini 2016), or in

*Correspondence: scuomo@unisa.it
[1] University of Salerno, Fisciano, Italy
Full list of author information is available at the end of the article

some cases in full-scale flume experiments (De Natale et al. 1999; Bugnion et al. 2012).

In general, the reduced-scale laboratory tests have been extensively used to derive and to validate the empirical formulations most used to assess the peak impact pressure in the design of protection measures against landslide (Proske et al. 2011). The existing empirical methods can be classified into three groups: (i) hydro-static methods, which require only flow density and thickness for evaluating the maximum impact pressure (Scotton and Deganutti 1997; Schieldl et al. 2013); (ii) hydro-dynamic methods, based on flow density and the square velocity of the flow (Bugnion et al. 2012; Canelli et al. 2012); (iii) mixed methods, that accounts for both the static and the dynamic components of the flow (Arattano and Franzi 2003; Hübl et al. 2009; Armanini et al. 2011; Cui et al. 2015; He et al. 2016; Vagnon 2020). The weak point is that all the empirical formulations greatly depend on empirical coefficients which are difficult to estimate in the practical applications due to their wide range of variation. Common to those approaches are the following assumptions: (i) the impact load is assumed to be totally transferred to the structure without any dissipation during the impact, and (ii) the size, stiffness and inertial resistance of the artificial barrier are not considered (Vagnon and Segalini 2016). These assumptions generally lead to safe assessment of the peak impact force but with large overestimation in the barrier design. Hence, some enhancements will be proposed in this paper on both these topics.

The present work investigates the impact mechanisms of flow-like landslides against artificial barriers in full-scale realistic scenarios. A Conceptual Model of LSI is firstly proposed. Then, a new empirical method is casted to evaluate the peak impact horizontal force and the reduction in the kinetic energy of the flow. The new empirical formulation is calibrated with a set of numerical results, achieved by applying the MPM approach to analyse the hydro-mechanical interaction of saturated flows with different types of barriers. The validation of the empirical formulation is pursued with reference to a large dataset containing field evidence of impact problems for real debris flows. Finally, the novel empirical formulation is compared with those from the literature and its potential and limitations are discussed.

Framework

It is assumed that a flow-like landslide impacts against a rigid protection barrier fixed to the base ground (Fig. 1a). The landslide body has the following features: unitary width, length L_1, depth h, density of the mixture ρ_m, initial uniform velocity v_0, pore-water pressure p_L and friction coefficient along the base ground equal to $\tan\varphi_b$. In real cases, the barrier is often built as a reinforced concrete vertical wall or an embankment with a steep inclined face at the impact side. For the sake of generality, here below we consider that the barrier is a trapezoid, with these geometric characteristics: bottom base B, top base b, height H, inclination of the impacted side β.

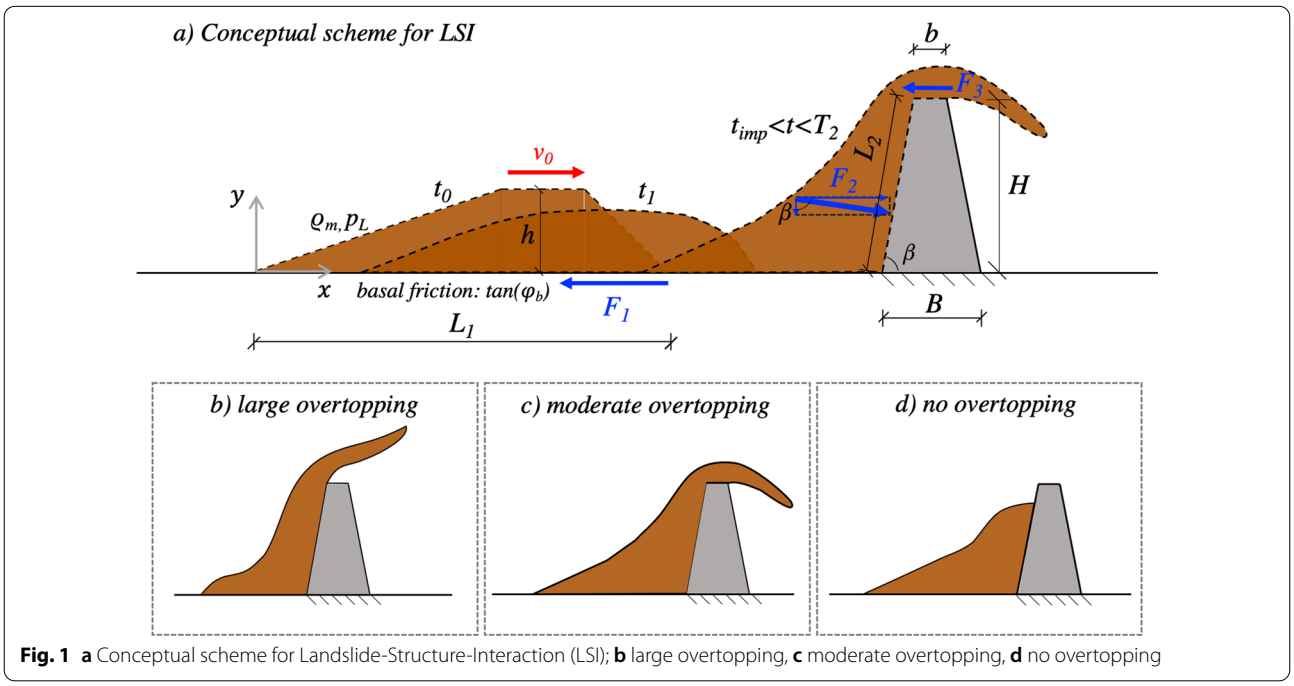

Fig. 1 **a** Conceptual scheme for Landslide-Structure-Interaction (LSI); **b** large overtopping, **c** moderate overtopping, **d** no overtopping

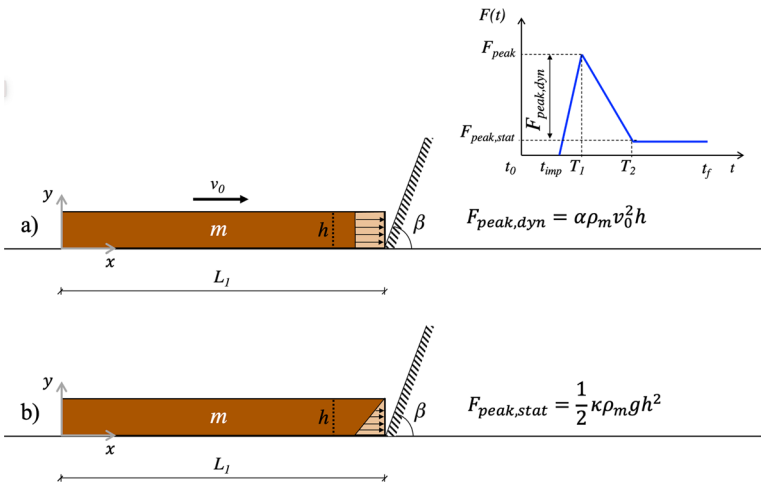

Fig. 2 Schematic of the impact problem in the proposed empirical model

The LSI problem is described through the following timelines: initial configuration (t_0), landslide propagation ($t_0 < t < t_{imp}$), impact of the landslide front (t_{imp}), time of the peak impact force (T_1), start of the inertial stage (T_2), end of LSI (t_f). Before the landslide reaches the barrier ($t_0 < t < t_{imp}$), i.e., during the propagation stage, the LSI problem is governed by the basal frictional force F_1, which acts along the bottom of the flow (L_1) and controls the reduction in flow velocity, resulting in a decrease of the impact forces. While the flow interacts with the barrier ($t_{imp} < t < T_2$), additional stresses (mostly orthogonal to the impacted surface, hence horizontal in many applications) are produced at the impacted side of the barrier. Many studies (e.g., Cui et al. 2015; Song et al. 2017) demonstrated that the total impact force–time history can be simplified as a triangular force impulse, from nil to the peak value and then down to a static value, usually with a rise time (T_1) much shorter than the decay time ($T_2 - T_1$).

According to the Newton's Third law of motion, the mutual impact forces (F_2) between the landslide and the barrier are equal and opposite. Such mutual stress makes the flow to decelerate. The evaluation of the impact forces applied on the inclined side of the barrier (L_2) is fundamental to design the structural characteristics of the barrier. It is worth noting that the flow may overtop the barrier during the impact, generating an additional force F_3 on the structure, mainly dependent on the flow-barrier frictional contact ($\tan\delta$). In a simplified approach, F_1 and F_3 could be neglected. Once F_1, F_2 and F_3 are given, the constraint reactions required at the base of the barrier can be computed. Thus, the ultimate strength of the foundation systems can be designed so that the barrier does not move. In practice, a solution is placing a base layer of soil with an assigned frictional resistance.

The expected LSI mechanisms, in a contest of landslide risk mitigation, must be distinguished among those with large (Fig. 1b) or moderate (Fig. 1c) flow overtopping of the barrier and that mechanism (Fig. 1d) which makes the flow to stop behind the barrier. Consistently with the literature (Faug 2015, among others), it is considered that the LSI dynamics is guided by the impact velocity and the height of the protection structure relative to the flow thickness. High flow velocity predisposes to the large (Fig. 1b) or moderate (Fig. 1c) overtopping depending on the height of the barrier. On the other hand, the taller is the barrier the more probable is that the flow is fully retained (Fig. 1d). However, LSI dynamics is also guided by landslide pore pressure (Cuomo et al. 2021), and this issue will be considered in the following.

Formulation of a novel empirical method

The landslide is here schematized as a rectangular with mass m, length L_1, depth h, unitary width, density ρ_m, initial velocity v_0 and it is supposed that the landslide is completely stopped by the barrier (i.e., $v(T_2) = 0$). The latter is assumed as fixed to the base ground and indefinitely high, thus all the landslide volume is supposed to be retained by the barrier (Fig. 1d).

Based on previous studies (Hungr et al. 1984; Scotton and Deganutti 1997; Kwan 2012), the peak lateral force F_{peak} (Eq. 1) exerted by the flow on the obstacle is calculated by the sum of a dynamic component $F_{peak,dyn}$ (Fig. 2a) and a height-dependent static component $F_{peak,stat}$ (Fig. 2b), as reported in Eqs. 2–3, respectively.

$$F_{peak} = F_{peak,dyn} + F_{peak,stat} \tag{1}$$

$$F_{peak,dyn} = \alpha \rho_m v_0^2 h \tag{2}$$

$$F_{peak,stat} = \frac{1}{2}\kappa \rho_m g h^2 \tag{3}$$

The empirical coefficient α has a wide range of values, ranging from 0.4 to 12 (Vagnon 2020), while the empirical static coefficient κ ranges from 9 to 11 as reported by Armanini (1997) or in the range 3–30 as observed by Scheidl et al. (2013) for $Fr < 3$. The static coefficient κ is suggested to be assumed equal to 1 (Ng et al. 2021) for saturated flows, which are fluidized due to the excess pore pressure developed inside the landslide at the impact. In this paper, the value of α is calibrated based on the MPM simulation of a selected set of realistic cases.

The landslide kinetic energy during the impact process is derived from its velocity variation over time until the impact process finishes (T_2). The impulse theorem (Eq. 4), where the impulse of the impact force is equal to the variation of linear momentum, the link between the impact force and velocity variation is obtained. Since the time-trend of the impact pressure is a piecewise function, the equations system reads as in Eq. 5. For sake of simplicity, it is assumed that $t_0 = t_{\text{imp}} = 0$.

$$I = \int_0^{T_2} F(t)dt = \int_{v_0}^{0} m dv \tag{4}$$

$$F(t) = \begin{cases} F_{peak} t/T_1 & 0 < t < T_1 \\ F_{peak}[1 - (F_{peak,dyn}/F_{peak}) \\ \quad (t - T_1)/(T_2 - T_1)] & T_1 < t < T_2 \end{cases} . \tag{5}$$

The reduction in landslide velocity is obtained from Eq. 6, by solving the integrals in Eq. 5 and replacing the term $F(t)$ with Eq. 4. Thus, the flow velocity over time (Eq. 7) and the corresponding kinetic energy (Eq. 8) can be computed.

$$\Delta v(t) = \begin{cases} \frac{F_{peak}}{2mT_1} t^2 & 0 < t < T_1 \\ \left[\frac{F_{peak}}{m} + \frac{F_{peak,dyn} T_1}{2m(T_2 - T_1)}\right] t \\ \quad - \frac{F_{peak,dyn}}{2m(T_2 - T_1)} t^2 & T_1 < t < T_2 \end{cases} \tag{6}$$

$$v(t) = v_0 - \Delta v(t) \tag{7}$$

$$E_k(t) = \frac{1}{2} m v^2(t) \tag{8}$$

The impact period T_2 is obtained by using the impulse theorem, since the integral over time of the impact force (i.e., the impact impulse) is equal to the variation of linear momentum of the landslide (Eq. 4). The left side of Eq. 4 can be rewritten as reported in Eq. 9, where the right side corresponds to the area subtended by the piecewise function reported in Eq. 5 and plotted in Fig. 2a. Once known T_2 through Eq. 10, T_1 can be achieved in Eq. 11 by fixing the ratio $\tau = T_1/T_2$ (for example from experimental evidence). The description of the impact dynamics is complete.

$$\int_0^{T_2} F(t)dt = \frac{1}{2}\left(F_{peak} + F_{peak,stat} - \tau F_{peak,stat}\right) T_2 \tag{9}$$

$$T_2 = 2mv_0 / \left(F_{peak} + F_{peak,stat} - \tau F_{peak,stat}\right) \tag{10}$$

$$T_1 = \tau T_2 \tag{11}$$

Summing up, the primary unknown of such LSI model is T_2, while the quantities α, κ and τ, must be calibrated. Some examples are shown in Fig. 3 to highlight the effect of α, κ and τ on impact force and kinetic energy trend over time. The input quantities of the model are: $L_1 = 15\text{m}$; $h = 3\text{ m}$; $\rho_m = 1800\text{kg/m}^3$; $v_0 = 10\text{m/s}$. High values of α result in large peak forces, short impact time T_2 and rapid decrease of the kinetic energy of the flow. This means that α can be interpreted as a measure of system deformability, since the decreasing of T_2 with α means that the system is stiffer.

The empirical coefficient κ has similar behaviour compared to α, since high values of κ result in large peak forces and short time T_2. However, the coefficient κ has a minor influence on the system response compared to the coefficient α (as evident in Fig. 3) and its determination is quite complicated. For this reason, the static component of the impact force could be disregarded ($\kappa = 0$), using only the coefficient α for the assessment of the impact scenario. For fluidized flows the assumption of $\kappa = 1$ is preferable (as suggested by Ng et al. 2021) therefore also this value will be employed for the calibration of the model.

Finally, the ratio τ governs the occurrence of the peak time, and thus the shape of the impact force trend. In terms of flow kinetic energy dissipation, the higher the ratio τ, the steeper the dissipation trend up to T_1 and the slower the energy reduction between T_1 and T_2. In a sense, the parameter τ can be interpreted as a measure of the impulsiveness of the impact loading.

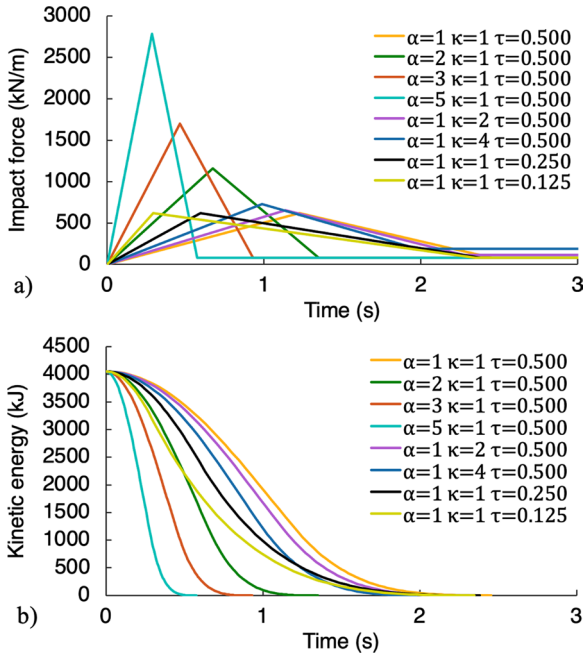

Fig. 3 Dependence of the impact force (**a**) and landslide kinetic energy (**b**) on model parameters

Calibration via MPM modelling

Input and data

The Material Point Method is an appropriate modelling alternative for large deformation problems. The Lagrangian points (named Material Points) are free to move across a fixed mesh, which schematizes the domain where the materials are in their initial configuration and where they will move during the deformation process. At each time step, the governing equations are solved on the mesh, but then all the stress–strain variables are saved in the MPs.

To schematize the LSI problem in a realistic way, the build-up of pore water pressure in the flow material during the impact is considered as well as the hydro-mechanical coupled behaviour and the yielding of the flow material. For a saturated porous material, each MP reproduces a volume of the mixture V, given by the sum of the solid V_S and liquid V_L phases volumes. Each MP stores the information about both the solid and liquid phases. This is called *two-phase single-point* formulation (Jassim et al. 2013; Ceccato et al. 2018; Fern et al. 2019). The primary unknowns are the solid ($\mathbf{a}_S$) and the liquid acceleration ($\mathbf{a}_L$). From there, the velocity of solid and liquid phases are obtained. The MPs are moved with the kinematics of the solid skeleton during the computation. Details are reported in the "Appendix 1" and by Martinelli and Galavi (2022).

The landslide is modelled through the *two-phase single-point* formulation. The initial configuration of the landslide is meant to represent the shape of the flow at a certain time during propagation (Fig. 3), but it strongly depends on site-specific flow-path topography and geomorphological conditions. However, friction with the ground topography often result in a stronger higher front and weaker lower body and a tail of the mixture flow (Iverson 1997; Pudasaini and Fischer 2020; Thouret et al. 2020). Here, we consider a 45°-inclined front and a tail of length equal to three times the flow height. To consider different flow volumes, a i number of squares are placed between the head and tail portions. Given this shape, the landslide as the same volume of an equivalent rectangular with the same height h and a length $L_m = (2 + i) \cdot h$, and unitary width (Fig. 3). The flow is a saturated mixture with hydrostatic distribution of initial pore-water pressure. The landslide is assumed as approaching the barrier with a fixed geometric configuration and constant velocity, until the LSI starts. For the sake of simplicity, the flow basal frictional force F_1 (Fig. 1a) is assumed equal to zero in all cases, by means of a smooth contact. Although simplified, the landslide scheme resembles its main characteristics such as velocity, impact height, non-zero interstitial pressures and elasto-plastic behavior. The mechanical parameters of the landslide material are: ρ_m (density of the mixture) = 1800 kg/m^3; n (porosity) = 0.4; ϕ' (effective friction angle) = 20°; c' (effective cohesion) = 0; E' (Young modulus) = 2 MPa; ν (Poisson's ratio) = 0.25; k_{sat} (hydraulic conductivity) = 10^{-4} m/s; μ_L (liquid viscosity) = 10^{-6} kPa s; K_L (liquid bulk modulus) = 30 MPa.

The barrier is modelled through the *one-phase single-point* MPM formulation ("Appendix 1"). For the barrier it is assumed: non-porous material, base fixed to the ground and rigid behaviour. This last hypothesis relates to the construction mode typically used for such barriers (Cuomo et al. 2020).

Different impact scenarios are investigated. The geometric features of both the landslide and the barrier are summarized in Table 1. It is worth noting that the case of an infinite wall is that considered in the literature empirical models. The expected impact mechanism (Table 1) is computed for each scenario, based on the diagram proposed by Faug (2015), with the Froude number (defined as $v/\sqrt{gh}$,) calculated considering that the impacted side of the barrier is inclined of β (i.e., $v = v_0 \sin \beta$). From that, the expected amount of overtopping is inferred.

Examples of the geometric schematization (fixed background mesh) in the MPM model are provided in Fig. 4. The computational fixed mesh is always unstructured, namely made of triangles with different sizes, and finer in the zone where the LSI occurs. For instance, in Fig. 4a, it is made of 20,515 triangular 3-noded elements with dimensions ranging from 0.20 to 1.00 m. On the other hand, the number of MPs is

Table 1 Selected impact scenarios

ID	L_1 (m)	L_m (m)	i (−)	h (m)	V_1 (m^3/m)	$v_{0,1}$ (m/s)	β (°)	d (m)	L_2 (m)	B (m)	b (m)	H (m)	Fr (−)	H/h (−)	Impact mechanism*	Expected overtopping^
1	21	15	3	3	45	10	60	3	6.95	11	4	6	1.60	2	Standing jump	Large
2	21	15	3	3	45	20	60	3	6.95	11	4	6	3.19	2	Airborne jet	Large
3	21	15	3	3	45	10	90	3	∞	–	–	∞	1.84	∞	N/D	Nil
4	47	45	43	1	45	10	60	3	6.95	11	4	6	2.76	6	Bore	Moderate
5	21	15	3	3	45	5	60	3	6.95	11	4	6	0.80	2	Dead zone	Nil
6	21	15	3	3	45	15	60	3	6.95	11	4	6	2.40	2	Airborne jet	Large
7	21	15	5	3	63	10	60	3	6.95	11	4	6	1.60	2	Standing jump	Large
8	21	15	3	3	45	10	80	3	6.08	8.5	6.5	6	1.82	2	Standing jump	Large
9	21	15	1	4	48	10	60	3	6.95	11	4	6	1.38	2	Standing jump	Large

* From the study of Faug (2015); ^ from the conceptual scheme in Fig. 1

9535 for case 3 (Fig. 4b), while equal to 24,107 for case 4 (Fig. 4f).

Examples of MPM results

The numerical MPM analyses evidently allow the simultaneous simulation of flow propagation and flow-structure interaction. One of the main advantages of the MPM modelling is the possibility of monitoring important quantities of the flow during impact, such as stresses, strains, pore-water pressure, velocity, depth, etc. For example, in Fig. 5 is shown the spatio-temporal evolution of landslide velocity field. The cases 1, 2, 4 and 5 of Table 1 are chosen since they are characterized by different impact mechanisms and consequently by diverse amount of overtopping expected. The numerical simulation of these cases can validate the conceptual scheme reported in Fig. 1, as it is possible to compute the percentage of volume retained by the barrier ($V_{f,LH}/V_1$), namely the left hand accumulated landslide volume ($V_{f,LH}$) divided to the landslide volume (V_1). This is an important issue that must be considered for the design of the protection barriers.

Specifically, it emerges that for case 1 (Fig. 5a) the impact mechanism is a standing jump with large overtopping. Here, a part of the incoming flow overtops the barrier, forming a jet with high kinetic energy. Moreover, during the formation of the jet, the velocity of the flow upstream of the barrier is almost zero ($t=3$ s). Then, the flow has lost most of the initial kinetic energy and therefore goes back, also due to the presence of a smooth contact along the ground base. Completely different is case 5 (Fig. 5b), where the flow is characterized by a lower initial velocity. The impact mechanism here is the formation of a dead zone and all the flow is completely blocked by the barrier.

Figure 5c reports the velocity distribution of the case 2 with a huge initial kinetic energy of the flow. The barrier cannot stop the propagation of the landslide and a very prolonged jet with high energy is formed after the impact thus the amount of material that is retained by the barrier is quite smaller than the standing jump cases (large overtopping). Interesting is also the case of a shallow flow (case 4 in Fig. 5d), where the flow hits the barrier and then withdraws in unsteady conditions (bore impact mechanism). The flow does not have enough energy to overtop the barrier and therefore falls downward creating some turbulence in the remaining part of the incoming flow ($t>3$ s).

In Fig. 6 the Landslide-Structure-Interaction dynamic process is explained well. The peak of the horizontal and vertical components of the impact force ($F_{2,x}$ and $F_{2,y}$, respectively in Fig. 4a and b) are quite different in all the cases considered. In particular, a clear peak force is attained for the cases 2, 3 and 6. The higher is the flow velocity (or the steeper the barrier), the higher is the peak force. Conversely, the cases 4 and 5 does not show any distinct peak, where the impact forces are very limited. The frictional force along the top of the barrier (F_3), which is caused by landslide overtopping, is also illustrated in Fig. 6c. The highest F_3 is computed in the case 2, where the retained volume ($V_{f,LH}$) is the smallest. This force can also have a negative sign when the flow goes upstream, instead of flowing beyond the barrier.

The kinetic energy of the incoming flow (E_k) is plotted in Fig. 7. For a more comprehensive comparison, the curves are normalized by the initial kinetic energy of the flow ($E_{k,0}$). All the curves (except for case 4) show a sudden reduction, reaching the minimum value at approximately $t \cong 2s$ and, after that, the energy increases again as the formed jet takes the downward direction. This means that, during the flow, the kinetic energy is transformed to

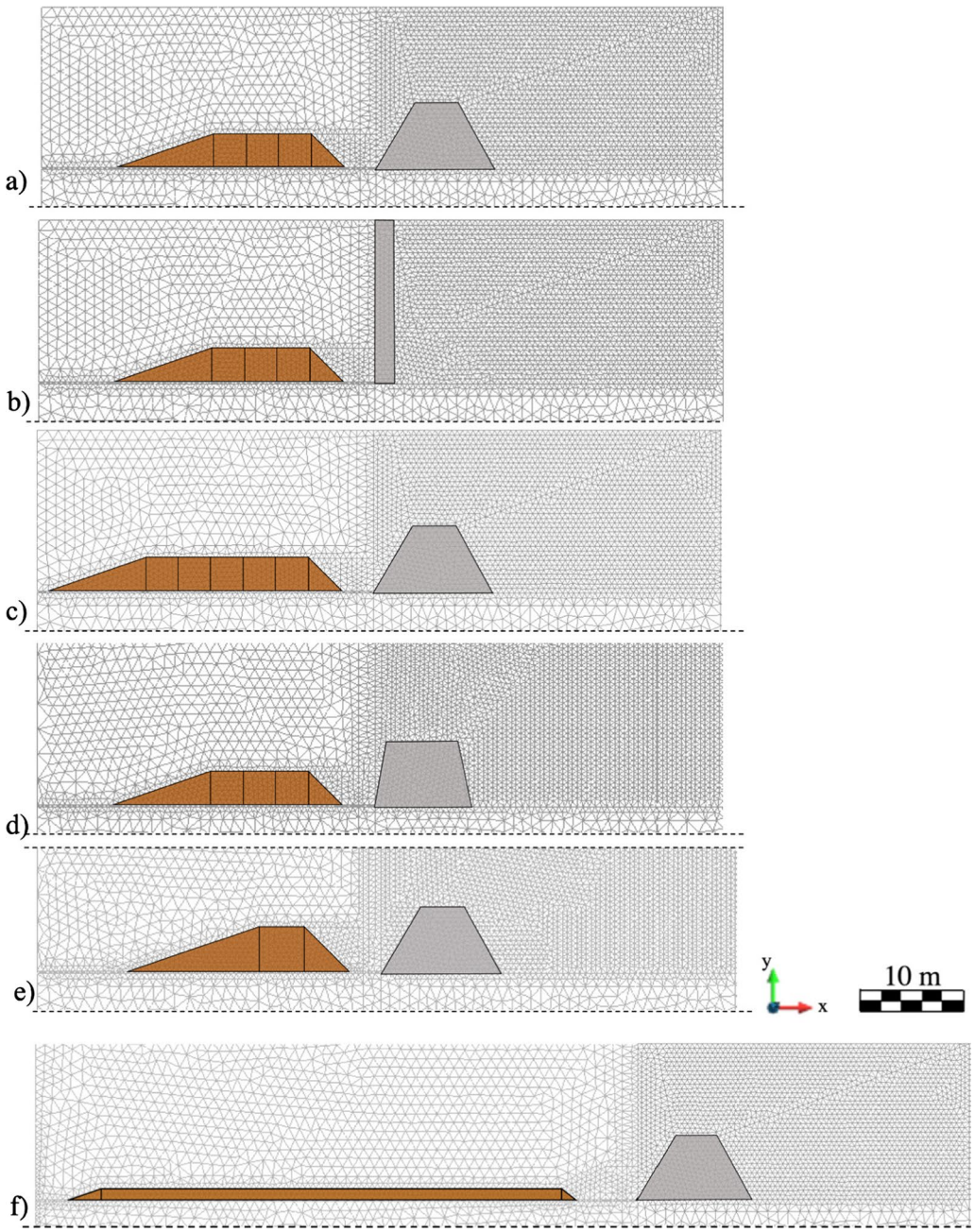

Fig. 4 Schematization of the problem in the numerical MPM model: **a** cases 1, 2, 5, 6; **b** case 3; **c** case 7; **d** case 8; **e** case 9; **f** case 4

potential energy. For $t > 2s$ all the trends are very different, since the curves represent the kinetic energy of the overcoming jet (especially for case 2) combined with the energy of the reflecting flow (especially for cases 3 and 5). The behavior of case 4 is completely different: it is characterized by a slower and constant reduction of the energy as the impact mechanism does not induce the formation of any jet.

Calibration results

The calibration of the empirical model principally focuses on the evaluation of the coefficients τ and α. The parameter τ is obtained by imposing the equivalence between T_1 calculated from Eq. 11, and T_1 obtained from the MPM simulations. The coefficient α relates to relevant features of the flow such as the grain size distribution, the barrier type and the flow-structure interaction mechanism such

as the formation of vertical jet-like wave at the impact (Canelli et al. 2012). As reported in the literature, this parameter can vary in a wide range (between 0.4 and 12), often leading to an excessive overestimation of the design impact load. However, many authors (Hübl et al. 2009; Proske et al. 2011; Scheidl et al. 2013; Cui et al. 2015; Vagnon 2020) developed a power law relationship between the coefficient α and the Froude number (Fr), as reported in Eq. 12.

$$\alpha = a_1 Fr^{a_2} \tag{12}$$

The evaluation of the coefficients a_1 and a_2 requires at least two numerical simulations with different Froude number. All the cases of Table 1 (except for cases 4 and 5, neglected due to the impossibility of identifying a unique peak value) are used for the calibration of the model. The case 1b is added with a different soil porosity. Globally, the influence of soil porosity n, landslide thickness h, landslide volume V_1, initial velocity $v_{1,0}$ and the barrier side inclination β are considered (Table 2).

Two calibration procedures were followed. The first neglects the static component of the impact force, thus the model can be considered purely hydro-dynamic. The other one assumes an empirical static coefficient κ equal to 1, that is more plausible for saturated flows. In the latter case, the peak impact force resulting from the MPM simulations was depurated of the static component ($0.5\rho_m g h^2$) for obtaining the dynamic one. The best fit values are $a_1 = 1.781$ and $a_2 = -0.515$ for $\kappa = 0$ (Eq. 13) and $a_1 = 1.432$ and $a_2 = -0.365$ for $\kappa = 1$ (Eq. 14). The calibrated value for τ is 0.14 for all the cases. The results show a good fitting with the $\alpha - Fr$ curve for all the impact scenarios, and it is relevant that also the trend over time of the impact force is reproduced quite faithfully for both. $\kappa = 0$ (Fig. 8a) and $\kappa = 1$ (Fig. 8c).

$$F_{peak} = 1.781 Fr^{-0.515} \rho_m v_{1,0}^2 h \tag{13}$$

$$F_{peak} = 1.432 Fr^{-0.365} \rho_m v_{1,0}^2 h + 0.5 \rho_m g h^2 \tag{14}$$

Besides achieving a good correspondence with the impact forces, the trend of flow kinetic energy was computed (Eq. 8) for the impact scenarios (Fig. 8b and d), giving for instance better agreement for the case 1 than the case 2. In the latter case, this is explained by the fact that high energy of the flow produces a more elongated jet, which cannot be reproduced by a simplified empirical method. The flow kinetic energy computed via empirical method is always lower than that computed through MPM (apart from case 7). This is mostly linked to the simplifying hypothesis of neglecting the static component of the impact force. However, it is a safe approximation, to be considered acceptable in the practice.

The output of the proposed empirical method are compared with the numerical results as it concerns the most relevant factors in LSI for the case with $\kappa = 0$ (Fig. 9). A similar comparison for the case with $\kappa = 1$ was also performed with satisfactory results, and it is omitted here for the sake of the simplicity. Based on the above calibration, the values of F_{peak} and T_1 computed through the empirical method (Eqs. 2 and 11, respectively) fit very well the MPM numerical results for all the scenarios. On the other hand, it is observed that the impact period T_2 (computed from Eq. 10) is only slightly overestimated by the empirical method especially for those cases with higher velocities. In these cases, the empirical method is not able to consider the amount of material which overtops the barrier. In fact, as the mass m decreases, this material no longer contributes to the variation of the linear momentum of the landslide (Eq. 4), therefore a lower value of T_2 is expected from Eq. 10. Only if the empirical equation is applied to the condition of the indefinite wall (case 3), where the overtopping of the barrier is not allowed, then the empirically-computed time T_2 perfectly matches the MPM outcome. In this case, even the other calculated quantities correspond to those obtained from MPM since the indefinite wall most resemble the basic assumptions of the empirical model.

For the evaluation of the flow kinetic energy at the peak impact force time, i.e., $E_k(T_1)$, the empirical formulation provides lower values than MPM for the cases with $v_0 > 10$m/s, while there is an appreciable matching for the other cases. This is mainly caused by the inability of the simplified proposed method to consider the hydro-mechanical coupling and large deformations within the flow, which play a crucial role during the interaction with the obstacle.

Validation for a large dataset

The proposed empirical method is thoroughly validated towards the interpretation of a large dataset of real observations of flow-type landslides, achieved through a permanent monitoring station. The field dataset from Hong et al. (2015) includes thickness, density, channel width, volume of discharge, velocity and impact forces recorded in real time during debris flow events.

The data are relative to 139 historical events that took place between 1961 and 2000 in the Jiangjia Ravine basin, located in the Dongchuan area of Yunnan Province in China (Zhang and Xiong 1997; Kang et al. 2007; Hong et al. 2015). The bulk density ranges from 1600 to 2300 kg/m^3 with fluid concentration ranging from 0.15 to 0.6. The dataset is well suited for the validation purpose as wide ranges of the relevant features are

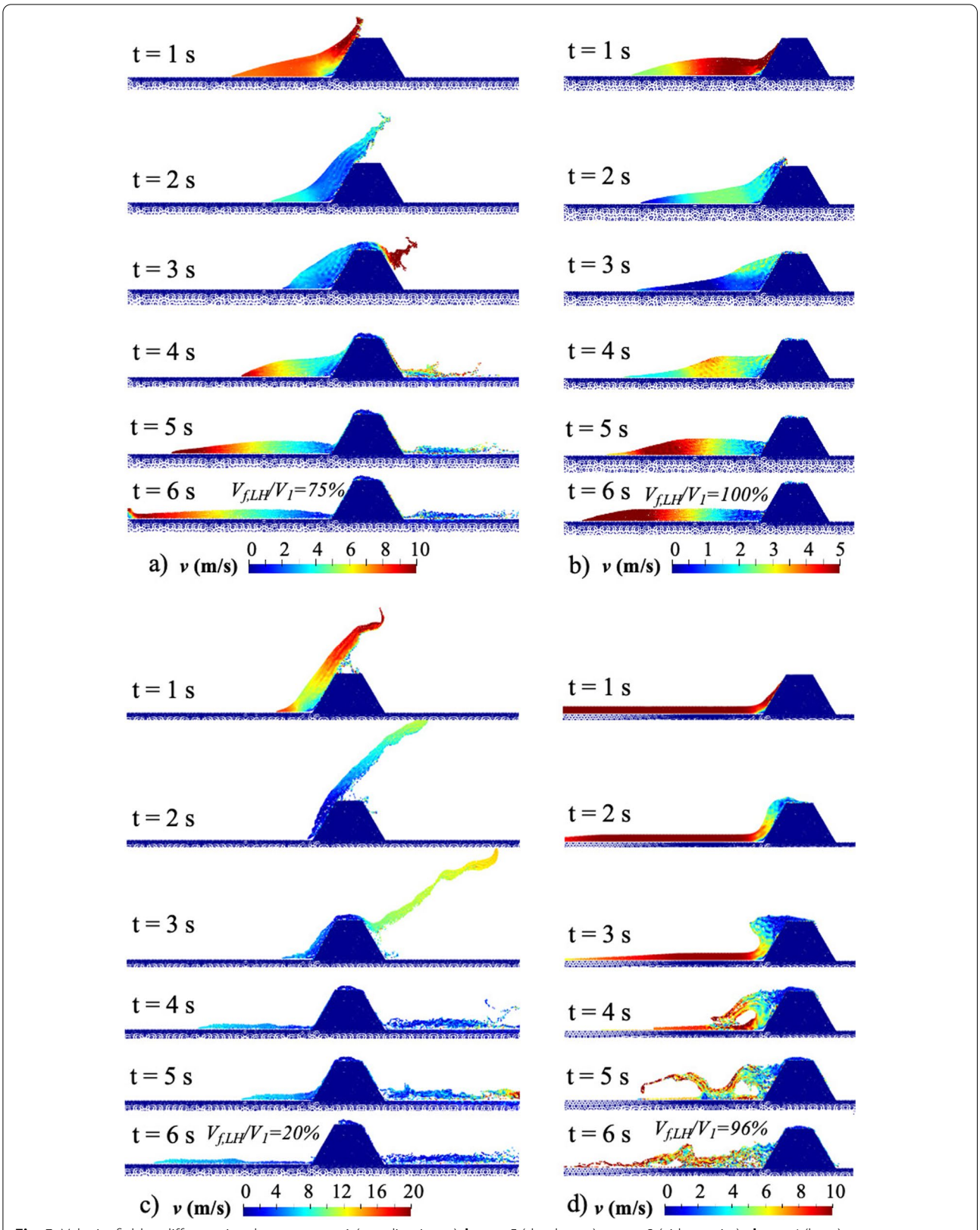

Fig. 5 Velocity field at different time lapses: **a** case 1 (standing jump); **b** case 5 (dead zone); **c** case 2 (airborne jet); **d** case 4 (bore)

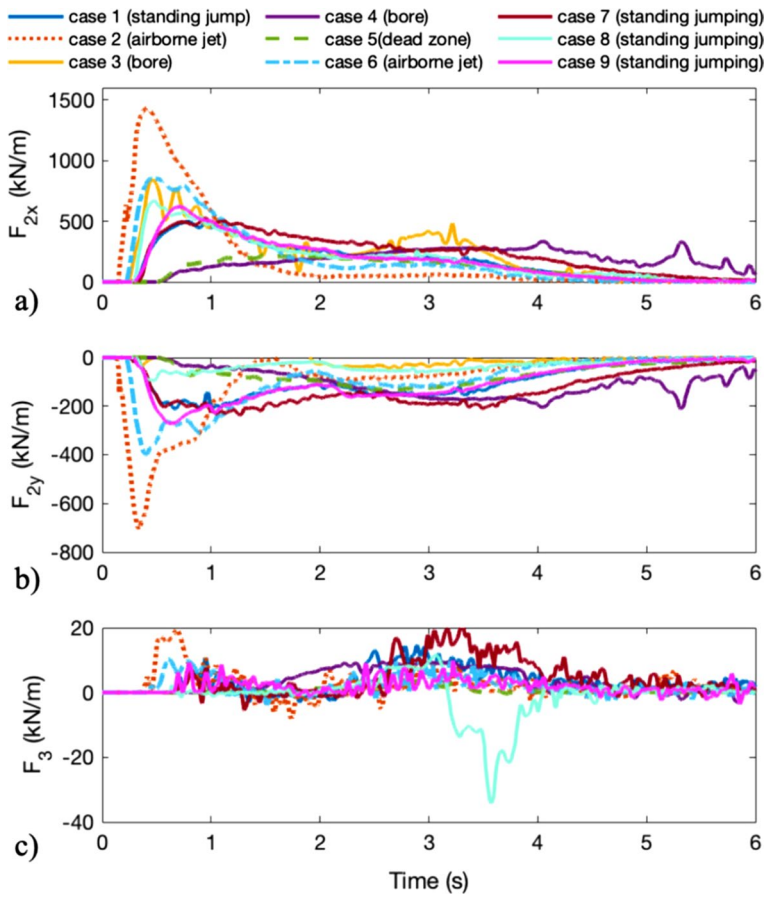

Fig. 6 Impact forces for different scenarios: **a** horizontal component of F_2; **b** vertical component of F_2, **c** F_3

considered such as: $v_0 = 3 - 14\text{m/s}$, $h = 0.2 - 2.7\text{m}$, $V = 269 - 1.75 \cdot 10^6\text{m}^3$ and $p_{peak} = 14 - 435\text{kPa}$.

The impact peak pressure is calculated through the calibrated power law for the peak force (Eq. 14) as follows: $p_{\text{peak}} = 1.432Fr^{-0.365}\rho_m v_{1,0}^2 + \rho_m gh$.The results are reported in Fig. 10 and show a very good correspondence with the field data, being the difference much less than 10% for most of the cases. In particular, the empirical model predicts quite well the peak of impact pressure for low values but showing some dispersion for values higher than 150 kPa. The statistical distribution of the error, obtained as the difference between the computed value and the measured value, shows that the median value is 10.7 kPa and the 90th percentile value is 37.65 kPa. The application of the numerical MPM model to such a large field dataset is beyond the scope this paper, while it could be a future development.

Discussion

A comparison between the presented methods is necessary to assess their strengths and weaknesses for analyzing the Landslide-Structure-Interaction.

MPM is an advanced numerical method and has proved to be reliable in predicting the impact force trend over time (Cuomo et al. 2021). Moreover, unlike field evidence or laboratory tests, the numerical results provide additional features, through the computation and time–space tracking of different quantities, such as stress, strain, pore pressure, solid and liquid velocities, which cannot be easily monitored or obtained in the field. Particularly focusing on LSI, many advantages come from using MPM. Primarily, it allows considering all such important features of the saturated flows, i.e. hydro-mechanical coupling and large deformations during propagation and impact. The accurate knowledge of the impact mechanism and so the evolution of flow depth and velocity is crucial for the design of mitigation countermeasures. For example, the accurate estimate of the length of the vertical jet must prevent that the retaining structure is overtopped by the flow, thus being ineffective. However, MPM suffers from some limitations, such as the high computational cost and until now the difficulty of being available in engineering practice.

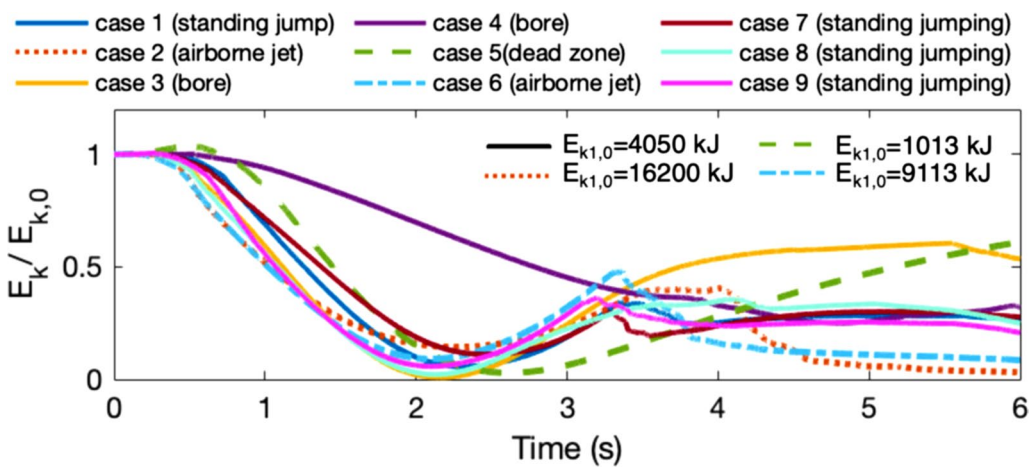

Fig. 7 Kinetic energy of the flow for different scenarios

Table 2 Selected parameters for the calibration of the empirical model through MPM simulations

	Flow type landslide				Barrier
ID	n (−)	h (m)	V_1 (m^3/m)	$v_{1,0}$ (m/s)	β (°)
1	0.5	3	45 ($i=3$)	10	60
1b	0.3	3	45 ($i=3$)	10	60
2	0.5	3	45 ($i=3$)	20	60
3	0.5	3	45 ($i=3$)	10	90
6	0.5	3	45 ($i=3$)	15	60
7	0.5	3	63 ($i=5$)	10	60
8	0.5	3	45 ($i=3$)	10	80
9	0.5	4	48 ($i=1$)	10	60

Empirical methods are more immediate and easier to use than MPM, since they provide an estimate of the impact quantities considering only the flow density, thickness and velocity as input and thus they could be preferable in the assessment of the LSI problems for design purposes.

Here, we apply some empirical methods available in the literature to interpret the field data of Hong et al. (2015), used already in Sect. 5, and we also applied the proposed method to the same dataset. The chosen empirical formulations are those of Hübl and Holzinger (2003), Armanini et al. (2011), Cui et al. (2015) and Vagnon (2020), all classifiable as mixed models (refer to Sect. 1).

In terms of peak pressure, the results of the empirical models of Armanini et al. (2011) and Vagnon (2020) have a low dispersion in the plot of Fig. 11, but with an overestimation of 61% and 35%, respectively. The formulations proposed by Hübl and Holzinger (2003) and Cui et al. (2015) are, in contrast, characterized by a quite relevant variability of the achieved results. The empirical model proposed in the present paper has the highest correspondence among the real data and the computed values, with a contained dispersion of the results. Some discrepancy of the results for very high velocities.

Can the present method be applied to the real multiphase debris flows? The answer is positive, especially in those cases where there are options on where to build one or more of these barriers. Hence, a quick direct method to assess the actions transferred by the flow to one barrier is helpful in the preparation of the whole mitigation plan. However, the LSI problem is not only a matter of peak impact pressure or kinetic energy decay. In fact, any barrier may suffer of flow overtopping, deformation/damage and shifting under the impact (and during the LSI). This is the reason that such flows and flow structure interactions are being simulated with the advanced multi-phase mass flow models such the MPM approach proposed here or through other advanced models (Mergili et al. 2020).

Concluding remarks

The present paper has proposed a conceptual framework, empirical and numerical models to analyse the impact of flow-like landslides against artificial barriers, focusing not only on the evaluation of the peak impact forces but also on the kinematics of the landslide during the whole impact process. A conceptual framework for the Landslide-Structure-Interaction (LSI) problem has been firstly introduced to better focus the main variables that govern the dynamics of the impact process. This framework has been then implemented in a novel empirical method.

The calibration of the new proposed empirical method has been performed using a set of numerical analyses

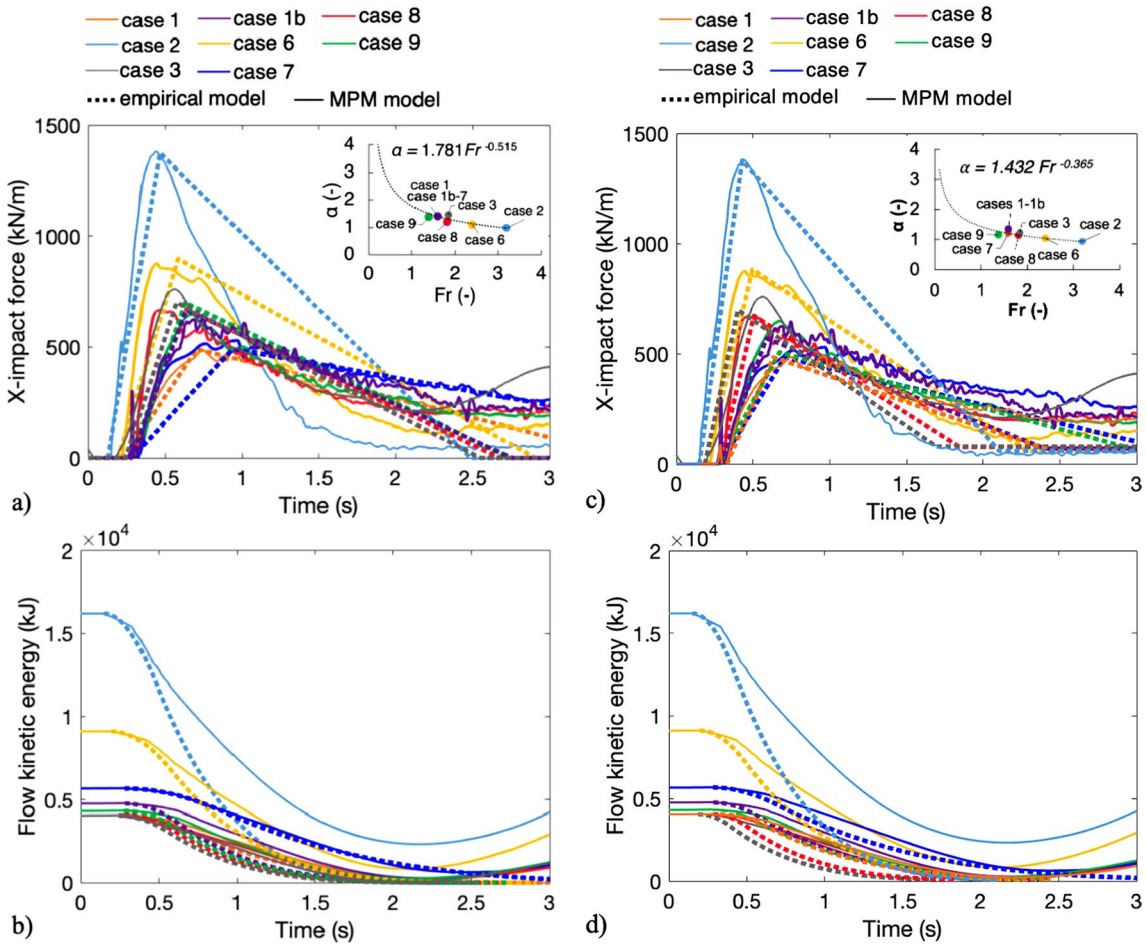

Fig. 8 Calibration of the empirical model through the MPM simulations (for the cases in Table 2): impact force (**a**) and kinetic energy (**b**) time trend for $\kappa = 0$ and impact force (**c**) and kinetic energy (**d**) time trend for $\kappa = 1$

conducted through the Material Point Method (MPM). The latter can easily reproduce a wide range of impact scenarios considering all the main features of LSI, such as the hydro-mechanical coupling, the soil large deformations and the presence of multi-materials. It has been possible to derive a new $\alpha - Fr$ power law relationship to derive the peak impact pressure. This formulation is different from those in the literature, which are typically calibrated on small-scale laboratory tests, thus giving an excessive overestimation in predicting the impact load that may results in a large increment of costs for structure construction.

The validation of the empirical method has been done referring to a vast dataset of real field evidence collected at Jiangjia Ravine (China). The achieved results are encouraging, showing a high correspondence between the output of the proposed empirical formulation and the measured field data. However, the estimated power law for the empirical model can lead to an underestimation of peak pressures for values larger than 350 kPa, so it must be used with caution. Nevertheless, some available literature methods have been also applied to the same database, and thus the advantages of the new method are outlined.

In conclusion, both the proposed numerical and empirical methods can appropriately simulate the physical phenomena. Particularly, the numerical MPM analyses evidently allow the simultaneous simulation of flow propagation and flow-structure interaction. On the other hand, generally good agreement between empirical model and MPM simulation indicates that both results are physically meaningful. Further research may be directed to an enhancement of the proposed empirical model considering the amount of material that may overtop the barrier, giving more accurate results for the analysis of the LSI problem.

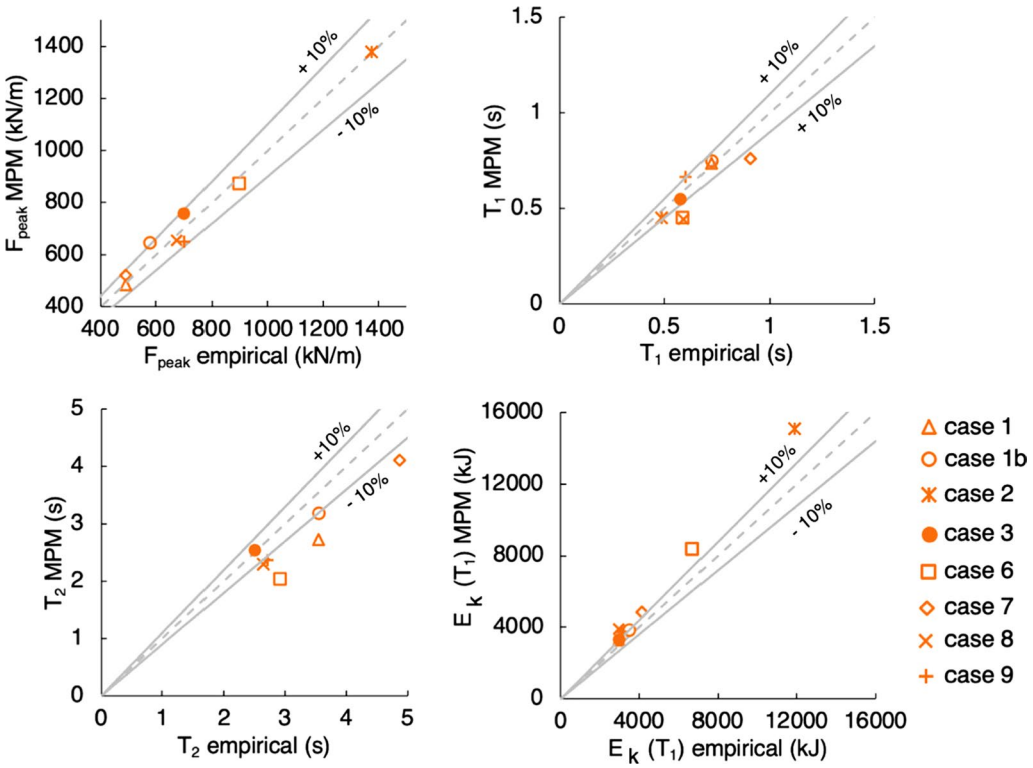

Fig. 9 Comparison of proposed empirical model with MPM results ($\kappa = 0$)

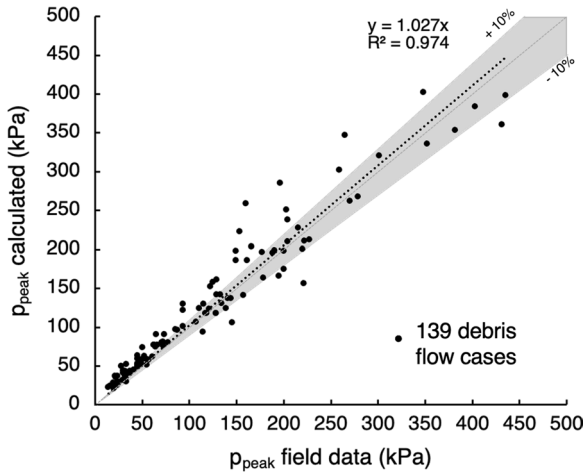

Fig. 10 Application of the proposed empirical model to the large field dataset (139 cases) collected by Hong et al. (2015)

Appendix 1: Material point method model equations

The equations to be solved concern the balance of dynamic momentum of solid and liquid phases, the mass balances, and the constitutive relationships of solid and liquid phases. The accelerations of the two phases are the primary unknowns: the solid acceleration $\mathbf{a}_S$, which is calculated from the dynamic momentum balance of the solid phase (Eq. 15), and the liquid acceleration $\mathbf{a}_L$, which is obtained by solving the dynamic momentum balance of the liquid phase (Eq. 16). The interaction force between solid and liquid phases is governed by Darcy's law (Eq. 17). Numerically, these equations are solved at grid nodes considering the Galerkin method (Luo et al. 2008) with standard nodal shape functions and their solutions are used to update the MPs velocities and momentum of each phase. The strain rate $\dot{\boldsymbol{\epsilon}}$ of MPs is computed from the nodal velocities obtained from the nodal momentum.

$$n_S \rho_S \mathbf{a}_S = \nabla \cdot (\sigma - n p_L \mathbf{I}) + (\rho_m - n\rho_L)\mathbf{b} + \mathbf{f}_d \quad (15)$$

$$\rho_L \mathbf{a}_L = \nabla p_L - \mathbf{f}_d \quad (16)$$

$$\mathbf{f}_d = \frac{n\mu_L}{k}(\mathbf{v}_L - \mathbf{v}_S) \quad (17)$$

The resolution of solid and liquid constitutive laws (Eqs. 18 and 19) allows calculating the increment of effective stress $d\boldsymbol{\sigma}'$ and excess pore pressure dp_L, respectively. The mass balance equation of the solid skeleton is then

used to update the porosity of each MP (Eq. 20), while the total mass balance serves to compute the volumetric strain rate of the liquid phase (Eq. 21) since fluxes due to spatial variations of liquid mass are neglected ($\nabla n\rho_L = 0$).

$$\mathrm{d}\boldsymbol{\sigma}' = \mathbf{D} \cdot \mathrm{d}\boldsymbol{\varepsilon} \tag{18}$$

$$dp_L = \mathbf{K}_L \cdot \mathrm{d}\varepsilon_{\boldsymbol{vol}} \tag{19}$$

$$\frac{Dn}{Dt} = n_S \nabla \cdot \mathbf{v_S} = 0 \tag{20}$$

$$\frac{D\varepsilon_{vol}}{Dt} = \frac{n_S}{n} \nabla \cdot \mathbf{v_S} + \nabla \cdot \mathbf{v_L} \tag{21}$$

In the two-phase single-point formulation the liquid mass, and consequently the mass of the mixture, is not constant in each material point but can vary depending on porosity changes. Fluxes due to spatial variations of liquid mass are neglected and Darcy's law is used to model solid–liquid interaction forces. For this reason, this formulation is generally used in problems with small gradients of porosity, and laminar and stationary flow in slow velocity regime. However, this formulation proves to be suitable for studying flow-structured-interaction (Cuomo et al. 2021). The water is assumed linearly compressible via the bulk modulus of the fluid $\mathbf{K}_L$ and shear stresses in the liquid phase are neglected.

The current MPM code uses 3-node elements which suffer kinematic locking, which consists in the build-up of fictitious stiffness due to the inability to reproduce the correct deformation field (Mast et al. 2012). A technique used to mitigate volumetric locking is the strain smoothening technique, which consists of smoothing the volumetric strains over neighbouring cells. The reader can refer to Al-Kafaji (2013) for a detailed description.

Regarding the critical time step, the influence of permeability and liquid bulk modulus must be considered as well (Mieremet et al. 2016). In particular, the time step required for numerical stability is smaller in soil with lower permeability (Eq. 22).

$$\Delta t_{cr} = \min\left(\frac{d}{\sqrt{(E + K_L/n)/\rho_m}}; \frac{2(\rho_m + (1/n - 2)\rho_L)k_{sat}}{\rho_L g}\right) \tag{22}$$

The sliding modelling of the flowing mass on the rigid material is handled by a frictional Mohr–Coulomb strength criterion. The contact formulation was used to ensure that no interpenetration occurs, and the tangential forces are compatible with the shear strength along the contact. The reaction force acting on the structure at node j was calculated as in Eq. 23.

$$F_j(t) = m_{j,S}\Delta a_{S,contact} + m_{j,L}\Delta a_{L,contact} \tag{23}$$

The terms $\Delta a_{S,contact}$ and $\Delta a_{L,contact}$ are the change in acceleration induced by the contact formulation, for both solid and liquid phase, and $m_{i,S}$ and $m_{i,L}$ are the corresponding nodal masses. The total reaction force is the integral of the nodal reaction forces along the barrier.

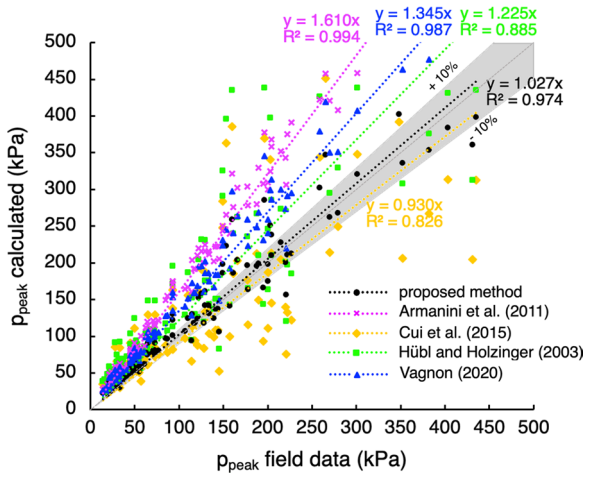

Fig. 11 The proposed empirical method compared to the results of some literature empirical methods in the interpretation of field dataset (139 cases) collected by Hong et al. (2015)

Appendix 2: A note on the role of pore water pressure

Selected results are shown in Figs. 12 and 13, where the spatial distribution of pore-water pressure is illustrated at different time instants of the propagation stage for all scenarios of Table 1. During the impact, the initial liquid pressure (< 30kPa) changes over time, with the maximum value in the first instants of the impact process ($t = 1$s) and later diminishing down to nil in some cases. However, the maximum value of pore water pressure ($p_{L,max}$) is dependent on the type of barrier. In fact, comparing an infinite wall (Fig. 12a) with a fixed artificial barrier (Fig. 12b), it follows that $p_{L,max}$ is higher in the first case, where the overtopping is impossible, and the impacted area of the barrier is larger than for the artificial barrier ($t = 1$ s). At $t = 2$s, the flow overtops the wall (Fig. 12a) or goes beyond the barrier forming a prolonged jet (Fig. 12b). Liquid pressure is decreasing, indicating that we are in the decay zone of the impact force diagram. Subsequently ($4\text{s} < t < 6\text{s}$), the flow loses more and more energy and falls down-

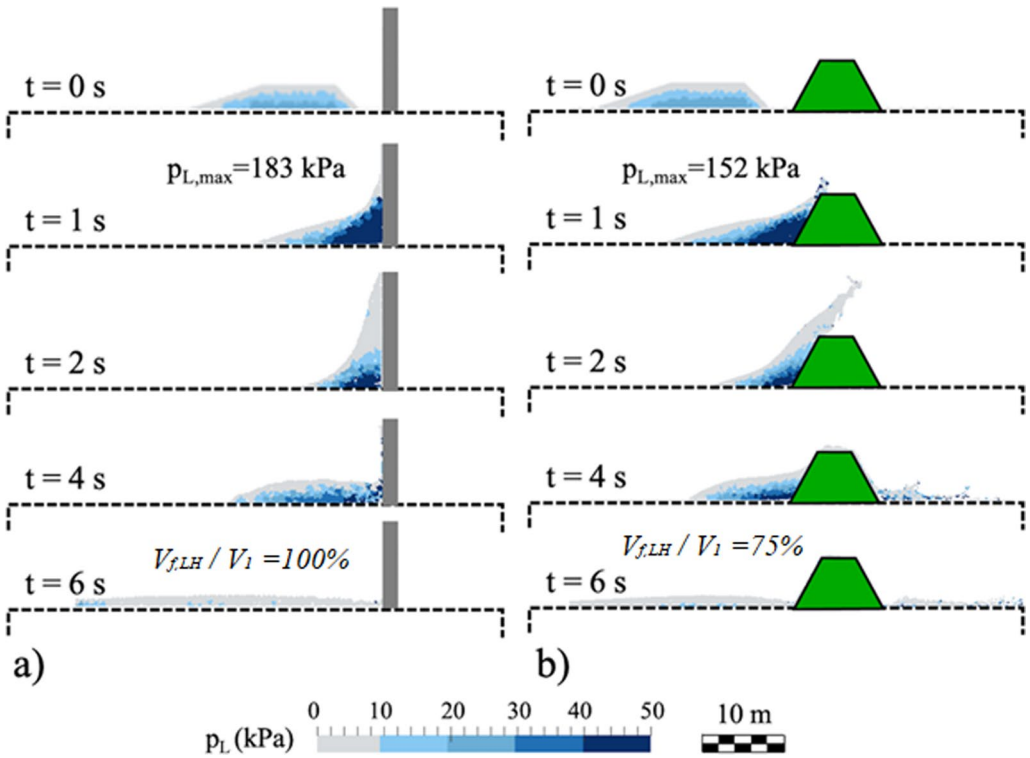

Fig. 12 Pore-water pressure distribution for: **a** infinite wall (case 3); **b** fixed barrier (case 1)

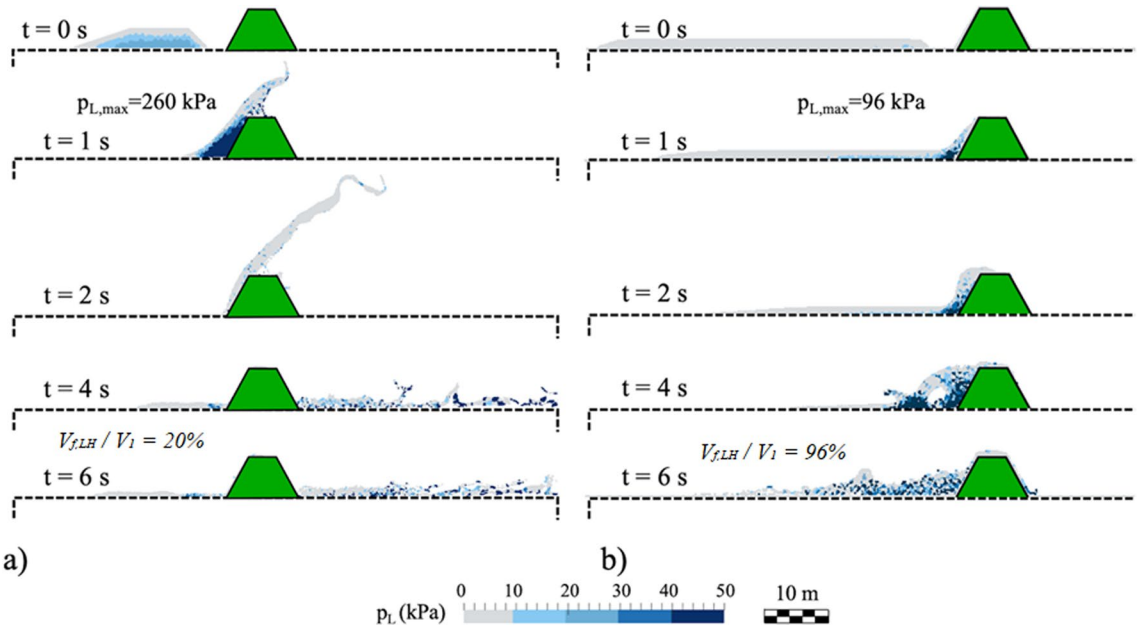

Fig. 13 Pore-water pressure distribution for different flows: **a** v_0 = 20 m/s (case 2); **b** H/h = 6 (case 4)

wards (similarly, in both cases).

The expected impact mechanism, as assessed from the use of the diagram by Faug (2015), is confirmed in both the cases. For the infinite vertical wall, the impact mechanism resembles the bores regime since a granular jump (named "bore") is formed which heads upstream of the wall. For the embankment barrier, the impact mechanism is the standing jump, which is similar to the bore regime but here a part of the incoming flow is able to overtop the barrier, forming a jet with very low energy.

Overall, the cases 1, 2 and 4 suggest a clear link between pore-water pressures at impact and the amount of overtopping flow mass, where larger pore-water pressures facilitate the overtopping of the barrier. This finding is also confirmed by previous experimental research (Song et al. 2017; Zhou et al. 2018).

Different flows are also considered to outline how MPM can reproduce the various impact mechanisms (Fig. 13). High flow velocities induce large values of $p_{L,max}$, which reaches 260 kPa (Fig. 13a). In this case, the expected impact mechanism is an airborne jet (Table 1) and it is confirmed very well from the numerical simulation. A very prolonged jet with high energy is formed after the impact, thus the amount of material that is retained by the barrier is much smaller than the standing jump case. Completely different is the case of a shallow flow (Fig. 13b), where the flow hits the obstacle and propagates upstream in unsteady conditions (bore regime).

Abbreviations

$a_1(-)$: Coefficient of the power law; $a_2(-)$: Coefficient of the power law; $\mathbf{a}_L\,(\mathrm{m/s^2})$: Liquid acceleration; $\mathbf{a}_S\,(\mathrm{m/s^2})$: Solid acceleration; B(m): Greater base of the barrier; b(m): Top base of the barrier; $\mathbf{b}$(kPa): Body force vector; c'(kPa) : Effective cohesion; d(m): Distance between landslide and barrier; $\mathbf{D}$(kPa): Tangent stiffness matrix; dp_L(kPa): Excess pore pressure; $d\boldsymbol{\sigma}'$(kPa): Increment of effective stress; E(kPa): Young modulus of soil; E_k(kJ): Kinetic energy of the landslide; F_1(kN/m): Contact force along the base of the flow; F_2(kN/m) : Impact force along the side of the barrier; F_3(kN/m): Contact force along the smaller base of the barrier; $F_{peak,dyn}$(kN/m): Dynamic peak impact force; $F_{peak,stat}$(kN/m): Static peak impact force; $Fr(-)$: Froude number; $\mathbf{f}_d$(kPa) : Drag force vector; $\boldsymbol{g}\,(\mathrm{m/s^2})$: Gravity vector; k_{sat}(m/s): Saturated hydraulic conductivity; $\mathbf{K}_L$(kPa): Elastic bulk modulus of the liquid; h(m): Flow heigth; H(m): Barrier heigth; LSI: Landslide-Structure-Interaction; L_1(m): Flow length; L_2(m): Length of barrier's lateral side; MPM: Material Point Method; m(kg): Landslide mass; $n(-)$: Porosity; p_L(kPa): Liquid pressure; t(s): Time; t_0(s): Initial reference time; t_{imp}(s): Time related to LSI beginning; t_f(s): Final time of LSI; T_1(s): Time related to the peak impact force; T_2(s): Final time of impact phase; $V_1\,(\mathrm{m^3})$: Volume of the mixture; $V_L\,(\mathrm{m^3})$: Liquid phase volume; $V_S\,(\mathrm{m^3})$: Solid phase volume; $V_{f,LH}\,(\mathrm{m^3})$: Volume retained by the barrier; $\mathbf{v}_L$(m/s): Liquid velocity vector; $\mathbf{v}_S$(m/s): Solid velocity vector; $\mathbf{v}_0$(m/s): Landslide initial velocity; x(m): Horizontal Cartesian coordinate; $y(m)$: Vertical Cartesian coordinate; $\boldsymbol{\alpha}(-)$: Dynamic impact coefficient; $\boldsymbol{\tau}(-)$: Ratio between T_1 and T_2; $\beta(°)$: Angle between lateral side and base of the barrier; $\Delta a_{S,contact}$: Change in solid phase acceleration induced by the contact formulation; $\Delta a_{L,contact}$: Change in liquid phase acceleration induced by the contact formulation; $\Delta t_{cr}(-)$: Critical time step; $\delta(°)$: Contact friction angle between flow and barrier; $\boldsymbol{\varepsilon}(-)$: Strain tensor; $\kappa(-)$: Static impact coefficient; μ_L(kPa s): Liquid dynamic viscosity; $\upsilon(-)$: Poisson's ratio; $\rho_L\,(\mathrm{kg/m^3})$: Liquid density; $\rho_m\,(\mathrm{kg/m^3})$: Density of the mixture; $\rho_S\,(\mathrm{kg/m^3})$: Solid density; $\boldsymbol{\sigma}$(kPa): Total stress tensor of the mixture; $\dot{\boldsymbol{\sigma}}$(kPa/s) : Jaumann stress rate matrix; $\boldsymbol{\sigma}_n$(kPa): Normal stress; $\varphi'(°)$: Internal friction angle; $\psi(°)$: Dilatancy angle.

Acknowledgements

The research was developed within the framework of Industrial Partnership Ph.D. Course (POR Campania FSE 2014/2020). All the MPM simulations were performed using a version of Anura3D developed by Deltares.

Author contributions

ADP is responsible for conceptualization, data collection and numerical modelling. SC is responsible for the data collection, numerical modelling and the corresponding passages in the manuscript. MM is responsible for numerical modelling and conceptualization. The authors read and approved the final manuscript.

Funding

The research was supported by several Italian Research Projects funded by the Italian Education and Research Ministry such as: Project FARB 2017 "Numerical modelling and inverse analysis for flow-like landslides"; Project FARB 2014 "Large area analysis of triggering and propagation landslide susceptibility for flow-like landslides"; Project FARB 2012 "New Frontiers of advanced numerical simulation of destructive landslides".

Declarations

Competing interests

The authors declare that we have any competing financial interests.

Author details

[1]University of Salerno, Fisciano, Italy. [2]Deltares, Delft, Netherlands. [3]Technical University of Delft, Delft, Netherlands.

Received: 23 December 2021 Accepted: 3 April 2022
Published online: 15 April 2022

References

Al-Kafaji I (2013) Formulation of a dynamic material point method (MPM) for geomechanical problems. Ph.D. Thesis, University of Stuttgart

Arattano M, Franzi LJNH (2003) On the evaluation of debris flows dynamics by means of mathematical models. Nat Hazard 3(6):539–544

Armanini A (1997) On the dynamic impact of debris flows, Recent developments on debris flows. In: Armanini, Michiue (eds) Lecture notes in earth science, vol. 64. Berlin, Springer, pp 208–224

Armanini A, Larcher M, Odorizzi M (2011) Dynamic impact of a debris flow front against a vertical wall. In: Proceedings of the 5th international conference on debris-flow hazards mitigation: mechanics, prediction and assessment. Padua, Italy, pp 1041–1049

Ashwood W, Hungr O (2016) Estimating total resisting force in flexible barrier impacted by a granular avalanche using physical and numerical modeling. Can Geotech J 53(10):1700–1717

Bugnion L, McArdell BW, Bartelt P, Wendeler C (2012) Measurements of hillslope debris flow impact pressure on obstacles. Landslides 9(2):179–187

Bui HH, Fukagawa R (2013) An improved SPH method for saturated soils and its application to investigate the mechanisms of embankment failure: case of hydrostatic pore-water pressure. Int J Numer Anal Meth Geomech 37(1):31–50

Calvetti F, Di Prisco CG, Vairaktaris E (2017) DEM assessment of impact forces of dry granular masses on rigid barriers. Acta Geotech 12(1):129–144

Canelli L, Ferrero AM, Migliazza M, Segalini A (2012) Debris flow risk mitigation by the means of rigid and flexible barriers–experimental tests and impact analysis. Nat Hazard 12(5):1693–1699

Ceccato F, Yerro A, Martinelli M (2018) Modelling soil-water interaction with the material point method. Evaluation of single-point and double-point formulations. In: NUMGE, 25–29 June. Porto, Portugal

Cui P, Zeng C, Lei Y (2015) Experimental analysis on the impact force of viscous debris flow. Earth Surf Proc Land 40(12):1644–1655
Cuomo S, Prime N, Iannone A, Dufour F, Cascini L, Darve F (2013) Large deformation FEMLIP drained analysis of a vertical cut. Acta Geotech 8(2):125–136
Cuomo S, Moretti S, Frigo L, Aversa S (2020) Deformation mechanisms of deformable geosynthetics-reinforced barriers (DGRB) impacted by debris avalanches. Bull Eng Geol Env 79(2):659–672
Cuomo S, Perna AD, Martinelli M (2021) Material point method (MPM) hydro-mechanical modelling of flows impacting rigid walls. Can Geotech J 58(11):1730–1743
De Natale JS, Iverson RM, Major JJ, LaHusen RG, Fiegel GL, Duffy JD (1999) Experimental testing of flexible barriers for containment of debris flows. US Department of the Interior, US Geological Survey, Reston
Faug T (2015) Depth-averaged analytic solutions for free-surface granular flows impacting rigid walls down inclines. Phys Rev E 92(6):062310
Fern J, Rohe A, Soga K, Alonso E (2019) The material point method for geotechnical engineering: a practical guide. CRC Press
He S, Liu W, Li X (2016) Prediction of impact force of debris flows based on distribution and size of particles. Environ Earth Sci 75(4):298
Hong Y, Wang JP, Li DQ, Cao ZJ, Ng CWW, Cui P (2015) Statistical and probabilistic analyses of impact pressure and discharge of debris flow from 139 events during 1961 and 2000 at Jiangjia Ravine, China. Eng Geol 187:122–134
Hübl J, Holzinger G (2003) Entwicklung von Grundlagen zur Dimensionierung kronenoffener Bauwerke für die Geschiebebewirtschaftung in Wildbächen: Kleinmassstäbliche Modellversuche zur Wirkung von Murbrechern. WLS Report 50 Band 3, Institute of Mountain Risk Engineering (in German)
Hübl J, Suda J, Proske D, Kaitna R, Scheidl C (2009) Debris flow impact estimation. In: Proceedings of the 11th international symposium on water management and hydraulic engineering, Ohrid, Macedonia, vol 1, pp 1–5
Hungr O, Morgan GC, Kellerhals R (1984) Quantitative analysis of debris torrent hazards for design of remedial measures. Can Geotech J 21(4):663–677
Iverson RM (1997) The physics of debris flows. Rev Geophys 35(3):245–296
Jassim I, Stolle D, Vermeer P (2013) Two-phase dynamic analysis by material point method. Int J Numer Anal Methods Geomech 37(15):2502–2522
Kang ZC, Cui P, Wei FQ, He SF (2007) Data collection of observation of debris flows in Jiangjia Ravine, Dongchuan Debris Flow Observation and Research Station (1995–2000)
Kattel P, Kafle J, Fischer JT, Mergili M, Tuladhar BM, Pudasaini SP (2018) Interaction of two-phase debris flow with obstacles. Eng Geol 242:197–217
Kwan JSH (2012) Supplementary technical guidance on design of rigid debris-resisting barriers. In: GEO Report No. 270, Geotechnical Engineering Office, Civil Engineering and Development Department, Hong Kong SAR Government
Leonardi A, Wittel FK, Mendoza M, Vetter R, Herrmann HJ (2016) Particle–fluid–structure interaction for debris flow impact on flexible barriers. Comput Aided Civ Infrastruct Eng 31(5):323–333
Luo H, Baum JD, Löhner R (2008) A discontinuous Galerkin method based on a Taylor basis for the compressible flows on arbitrary grids. J Comput Phys 227(20):8875–8893
Martinelli M, Galavi V (2022) An explicit coupled MPM formulation to simulate penetration problems in soils using quadrilateral elements. Comput Geotech Comput Geotech 145:104697. https://doi.org/10.1016/j.compgeo.2022.104697
Mast CM, Mackenzie-Helnwein P, Arduino P, Miller GR, Shin W (2012) Mitigating kinematic locking in the material point method. J Comput Phys 231(16):5351–5373
Mergili M, Jaboyedoff M, Pullarello J, Pudasaini SP (2020) Back calculation of the 2017 Piz Cengalo-Bondo landslide cascade with ravaflow: what we can do and what we can learn. Nat Hazards Earth Syst Sci 20(2):505–520
Mieremet MMJ, Stolle DF, Ceccato F, Vuik C (2016) Numerical stability for modelling of dynamic two-phase interaction. Int J Numer Anal Methods Geomech 40(9):1284–1294
Moriguchi S, Borja RI, Yashima A, Sawada K (2009) Estimating the impact force generated by granular flow on a rigid obstruction. Acta Geotech 4(1):57–71
Ng CWW, Majeed U, Choi CE, De Silva WARK (2021) New impact equation using barrier Froude number for the design of dual rigid barriers against debris flows. Landslides 1–13
Pastor M, Haddad B, Sorbino G, Cuomo S, Drempetic V (2009) A depth-integrated, coupled SPH model for flow-like landslides and related phenomena. Int J Numer Anal Methods Geomech 33(2):143–172
Proske D, Suda J, Hübl J (2011) Debris flow impact estimation for breakers. Georisk 5(2):143–155
Pudasaini SP, Fischer JT (2020) A mechanical model for phase separation in debris flow. Int J Multiph Flow 129:103292
Scheidl C, Chiari M, Kaitna R, Müllegger M, Krawtschuk A, Zimmermann T, Proske D (2013) Analysing debris-flow impact models, based on a small scale modelling approach. Surv Geophys 34(1):121–140
Scotton P, Deganutti AM (1997) Phreatic line and dynamic impact in laboratory debris flow experiments
Song D, Ng CWW, Choi CE, Zhou GG, Kwan JS, Koo RCH (2017) Influence of debris flow solid fraction on rigid barrier impact. Can Geotech J 54(10):1421–1434
Teufelsbauer H, Wang Y, Pudasaini SP, Borja RI, Wu W (2011) DEM simulation of impact force exerted by granular flow on rigid structures. Acta Geotech 6(3):119–133
Thouret JC, Antoine S, Magill C, Ollier C (2020) Lahars and debris flows: Characteristics and impacts. Earth Sci Rev 201:103003
Vagnon F (2020) Design of active debris flow mitigation measures: a comprehensive analysis of existing impact models. Landslides 17(2):313–333
Vagnon F, Segalini A (2016) Debris flow impact estimation on a rigid barrier. Nat Hazard 16(7):1691–1697
Zhang J, Xiong G (1997) Data collection of kinematic observation of debris flows in Jiangjia Ravine, Dongchuan, Yunnan (1987–1994)
Zhou GGD, Song D, Choi CE, Pasuto A, Sun QC, Dai DF (2018) Surge impact behavior of granular flows: effects of water content. Landslides 15(4):695–709

Publisher's Note